On the interactions between the critical dimensionless numbers associated with multiphase flow in 3D porous media

Ming Fan, Virginia Tech; Laura E. Dalton, National Energy Technology Laboratory; James McClure, Nino Ripepi, Erik Westman, Virginia Tech; Dustin Crandall, National Energy Technology Laboratory; and Cheng Chen, Virginia Tech

Abstract

Multiphase flow in porous media is of great interest in many engineering applications, such as geologic carbon sequestration, enhanced oil recovery, and groundwater contamination and remediation. In order to advance the fundamental understanding of multiphase flow in complex three-dimensional (3D) porous media, the interactions between the critical dimensionless numbers, including the contact angle, viscosity ratio, and capillary (Ca) number, were investigated using X-ray micro-computed tomography (micro-CT) scanning and lattice Boltzmann (LB) modeling. In this study, the 3D pore structure information was extracted from micro-CT images and then used as interior boundary conditions of flow modeling in a pore-scale LB simulator to simulate multiphase flow within the pore space. A Berea sandstone sample was scanned in three sections, and then two-phase flow LB simulations were performed on each section. The LB-simulated water/CO_2 distributions agreed well with the micro-CT scanned images. Simulation results showed that a decreasing contact angle causes a decrease in wetting-fluid relative permeability and an increase in non-wetting fluid relative permeability. A rising Ca number increases both wetting and non-wetting fluid relative permeabilities because the higher inertial force favors the mobility of both fluids. An increasing viscosity ratio (the ratio of non-wetting fluid viscosity to wetting fluid viscosity) facilitates the increase of non-wetting fluid relative permeability and mitigates the reduction of wetting fluid relative permeability, when the contact angle decreases continuously. This is because the lubrication effect is stronger when the wetting fluid viscosity is reduced, leading to enhanced non-wetting fluid relative permeability. The reduced wetting phase viscosity is also favorable for the mobility of the wetting fluid. In the literature, most works studied the role of viscosity ratio when the contact angle was fixed. In contrast, the primary novel finding of this study is that the viscosity ratio affects the rate of change of the relative permeability curves for both phases when the contact angle changes continuously. To the best of our knowledge, it is the first time comprehensive interactions between these dimensionless numbers are demonstrated in a sandstone sample based on real 3D structures. We also investigated the role of the changes of flow direction and sample location on relative permeability curves. Simulation results showed that the change in non-wetting fluid relative permeability was larger when the flow direction was switched from vertical to horizontal, which indicated that there was stronger anisotropy in larger pore networks that were primarily occupied by the non-wetting fluid. The combination of micro-CT imaging and LB multiphase flow simulation is a promising tool for advancing fundamental understanding of the interactions between the critical dimensionless numbers that regulate multiphase flow in complicated 3D pore space. This study advances the fundamental understanding of the multiphysics processes associated with multiphase flow in geologic materials and provides insight into upscaling methodologies that account for the influence of pore-scale processes in core- and larger-scale modeling frameworks.

Keywords: lattice Boltzmann, multiphase flow, capillary number, viscosity ratio, contact angle

1. Introduction

Understanding multiphase flow in three-dimensional (3D) porous media is of significant interest in many engineering applications, such as geologic carbon sequestration (e.g., [20,21,58]) enhanced oil recovery [50], and groundwater contamination and remediation [41]. Multiphase flow in geologic formations is a complex process influenced by a large number of physical and geologic properties, among which relative permeability is one of the most important and thus has attracted the most attention. It has long been recognized that relative permeability is not only a function of fluid saturation [1], but also depends strongly on several other physical parameters such as contact angle, viscosity ratio, capillary (Ca) number, saturation history, and stress condition [9,44,45]. Therefore, advanced understanding of these physical parameters at the pore scale, as well as the complicated interactions between them, has important implications for accurate prediction of larger-scale multiphase transport processes, such as the migration and trapping of injected CO_2 in geologic reservoirs [62].

Based on U.S. Department of Energy (DOE)'s methodology [32], CO_2 storage resource estimate for saline formations is related to the microscopic displacement efficiency, E_d, which ranges from 0.35 to 0.76 in clastic formations over the 10% to 90% probability range. However, recent core analysis [62] at the DOE's National Energy Technology Laboratory (NETL) showed that some sandstones can have E_d significantly lower than 0.35 due to strong heterogeneity. The uncertainties associated with microscopic and macroscopic estimations of carbon storage imply that advanced studies of multiphase flow in geologic formations is critical to address the fundamental questions that remain unanswered. For example, what is the interaction between contact angle, Ca number, and CO_2/water viscosity ratio, as well as its role on larger-scale relative permeability curves in natural 3D geologic formations? This work aims to combine laboratory experiments with numerical modeling to address this fundamental question associated with multiphase flow during geologic carbon sequestration.

Relative permeability can be measured in the laboratory using core flooding experiments, including the steady-state and unsteady-state methods. In the steady-state method, two immiscible fluids are injected simultaneously at constant flow rates, and relative permeability is measured directly based on its definition after the pressure drop and flow rate stabilize [42]. However, the steady-state method is time consuming because it can take up to several hours or even several days to reach the desired equilibrium conditions [53]. On the other hand, the unsteady-state method, which is a displacement process, is relatively fast and can mimic the real flooding process in underground reservoirs. However, it is an indirect method and relative permeability is calculated rather than being measured directly, which can be greatly affected by measurement errors and uncertainties resulting from the varying capillary pressure gradient and saturation gradient [45,53]. Because of these practical challenges in laboratory experiments, direct pore-scale numerical modeling of multiphase flow based on digital rock images has become a powerful alternative approach to derive the relative permeability and to help interpret experimental measurements.

The numerical approaches to determine transport properties in the pore space can be divided into two primary categories, the network modelling and direct modeling methods [11]. In the pore network modeling method, a topologically representative network is first extracted from micro-CT images and then used for the computations of the governing transport equations [49,61]. The advantages of this method are faster computational speeds and infinite resolutions compared to the direct modeling method. However, it is challenging to generate geometrically equivalent pore networks and to discretize the pore space into simple geometrical objects such as nodes and bonds [52,63]. Compared to the network modeling method, the direct modeling method solves the flow

and transport governing equations directly using micro-CT images (or other digital images of the pore geometry, such as scanning electron microscopy) as the boundary conditions of flow modeling. One of the most widely used and successful direct modeling methods is the lattice Boltzmann (LB) method, which accommodates highly complex pore geometries and is straightforward to implement [14]. With improvements in computer power and developments of new computational platforms, such as graphical processing unit (GPU) enhanced parallel computations [22], large-scale, high-resolution numerical simulations based on the LB method have been possible to simulate multiphase flow in complex, 3D porous media [10,47,54,55].

Two-phase flow properties in porous media have been extensively studied using the LB method due to its capability in coping with irregular flow paths and modeling the behaviors of fluid-solid and fluid-fluid interactions. Li et al. [45] investigated the effects of Ca number, wettability, and viscosity ratio on the relative permeability through a sphere-packed porous medium based on the LB method. They found an increasing contact angle increased wetting fluid relative permeability while decreasing non-wetting fluid relative permeability; a larger viscosity ratio or Ca number increases the relative permeability of the non-wetting fluid, whereas it has a relatively lesser influence on that of the wetting fluid. A similar study [27] reported the same effect of increasing Ca numbers and viscosity ratios on the variation of relative permeability in a two-dimensional (2D) porous structure. In Ghassemi and Pak's work [31], the LB method was used to analyze the relationships between relative permeability and wetting fluid saturation in a 2D porous medium; they showed that the viscosity ratio had a much more remarkable effect on the relative permeability of the non-wetting fluid than the wetting fluid. Furthermore, studies on the effect of contact angle on relative permeability using the LB method [38,39] showed that wettability has a larger influence on the relative permeability of the non-wetting fluid. Although these previous pore-scale investigations of relative permeability based on the LB method have generated remarkable results, most of the pore structures are on the basis of man-made or idealized porous media, such as glass bead and polyethylene bead packs [43], computer-generated 3D sphere-packed porous media [38,45], and computer-generated 2D pore structures with solid and void blocks [27,31,39,64]. Moreover, most of the previous simulation works did not have direct comparisons with laboratory experiments, especially if the 2D or 3D pore geometries were generated by computer modeling. Direct, comprehensive analysis of multiphase flow properties in the complex 3D pore space of natural geologic formations, which is commonly encountered in geologic carbon storage processes, has become a crucial task. However, to the best of our knowledge, there have been no pore-scale numerical simulations reported in the literature to study the complicated interactions between contact angle, viscosity ratio, and Ca number associated with the multiphase flow within a pore geometry directly based on microstructural images of 3D natural rocks.

In this work, two-phase LB flow simulations were conducted directly based on the 3D pore structural information of a Berea sandstone sample, which was acquired by micro-CT scanning at the DOE's National Energy Technology Laboratory [25,26,60,62]. First, a two-phase core flooding experiment was conducted on the Berea sandstone at DOE's NETL. Second, the distribution of contact angles was measured at the pore scale using micro-CT scanning. Third, LB two-phase flow modeling was conducted using the CT images of the sandstone as internal boundaries of flow modeling, and the initial condition of the LB modeling matched the imbibition process in the X-ray CT scanning stage. The LB-simulated two-fluid distribution was then compared with the micro-CT scanned two-fluid distribution at the pore scale. Fourth, the influence of various combinations of contact angle, viscosity ratio, and Ca number on the relative

permeability curves of the CO_2-water-rock system was comprehensively investigated. This study also evaluated the role of fluid injection direction (horizontal vs. vertical, and upward vs. downward) and micro-scale heterogeneity (different locations of the computational domain center) on the relative permeability curves. The combination of micro-CT imaging and LB multiphase flow simulation based on real, 3D rock structures has the potential to advance fundamental understanding of the multiphysics processes associated with multiphase flow in geologic materials, which provides insights into upscaling methodologies to account for the influence of pore-scale processes in core- and larger-scale modeling frameworks.

2. Methods

2.1 Core flooding experiments and X-ray micro-CT imaging

The core flooding experiments and X-ray micro-CT scanning were conducted at DOE's NETL (**Fig. 1**). The Berea sandstone core sample was 1.6 inches in length and 0.25 inch in diameter, with a porosity of 24.2%. The relatively small sample diameter (0.25 inch) was because that the high CT scanning resolution (2.36 μm/pixel) limited the total sample size in order to achieve an optimal X-ray transmission ratio. The core flooding setup was connected to a pressure vessel containing the core sample and mounted on the sample stage in the micro-CT scanner. The core flooding experiment involved CO_2-saturated brine injection (Step 1), followed by a CO_2 injection (Step 2), and lastly a final brine injection (Step 3). This process was implemented to mimic the imbibition process that was accounted for in the initial condition of the LB model, which will be discussed later. The flowrate was 0.05 ml/min, and 10 pore volumes (3.1 ml) of each fluid in each step were injected through the sample. The flow rate led to Ca number of 6.6×10^{-8}, which was in the range (between 3×10^{-9} and 3×10^{-5}) of the Ca numbers encountered in CO_2 aquifer storage projects [62]. During the core flooding experiment, the pore pressure was 1,800 psi and the confining pressure was 2,100 psi. The flow-through temperature was 24°C for all injections. After Step 3, the sample was set to shut-in conditions, pore pressure was fixed at 1,800 psi, temperature was increased to the supercritical condition (48°C), and the sample sat for 24 hours before micro-CT scanning allowing CO_2 to transition from the liquid state and fluid distribution to settle in the steady state. For simplicity, hereafter we refer to the wetting fluid as water in the following sections of this paper, although it should be noted that the wetting fluid used in the laboratory experiment was CO_2 saturated 5 wt% KI brine. The addition of KI to the water enhanced the difference between X-ray attenuation of the CO_2 and brine, enabling accurate segmentation of the fluids from the digital CT images.

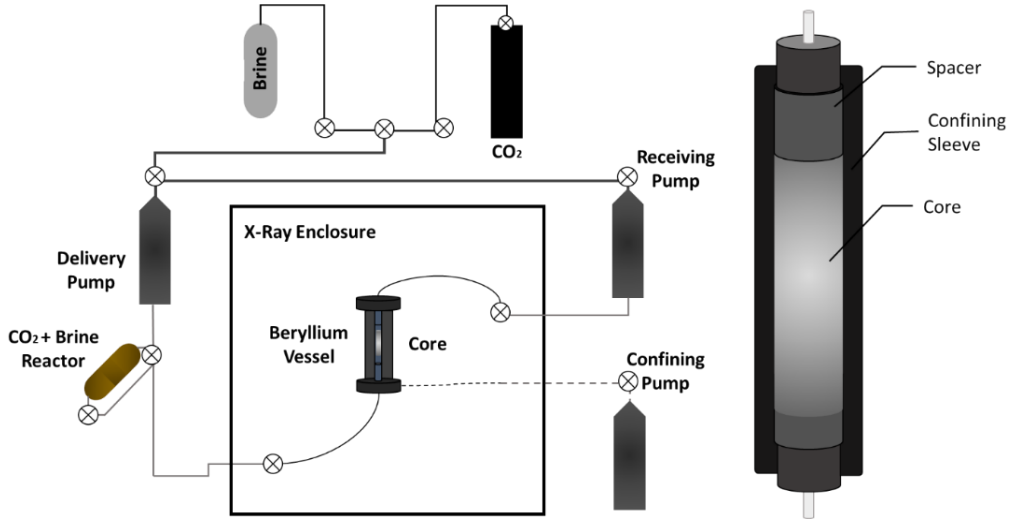

Fig. 1. U.S. DOE-NETL micro-CT laboratory setup.

2.2. Lattice Boltzmann method for multiphase flow simulation

The LB method is a numerical method for solving the Navier-Stokes equations and based on microscopic physical models and mesoscale kinetic equations [16,17,23,57]. In comparison with conventional fluid dynamic models, the LB method has many advantages. For example, it is explicit in the evolution equation, simple to implement, natural to parallelize [22,24,56], and easy to incorporate new physics such as interactions at fluid-solid interfaces [33,36,37].

A multiphase extension of Darcy's law is most typically used to describe two-fluid flow processes at the reservoir scale. The two-fluid system includes a wetting fluid (*w*) and a non-wetting fluid (*n*). The wetting fluid has a relatively higher affinity for the solid, and will tend to preferentially coat the rock surface as a result of the interfacial thermodynamics. As a consequence, the wetting and non-wetting fluid have a tendency to assume distinctly different configurations within the pore space. The relative permeability, k_{ri}, is introduced to account for these configurational effects, and the two-phase extension of Darcy's law is frequently written as

$$v_i = \left(k_{ri} / \mu_i\right) \mathbf{k} \cdot \left(-\nabla p + \rho_i \mathbf{g}\right) \tag{1}$$

where v_i, μ_i, ρ_i and k_{ri} are respectively the Darcy velocity, dynamic viscosity, density, and relative permeability associated with fluid i=*w*, *n*. $\mathbf{k}$ and ∇p are the permeability tensor and pressure gradient. External body forces such as gravity are accounted for by the vector $\mathbf{g}$. Since k_{ri} is a relative quantity, it is dimensionless and usually attains a value between zero and one, although it is possible to measure relative permeability values greater than one in certain situations.

This work relies on a multi-relaxation time (MRT) LB scheme formulated for two-fluid flow according to the "color" model, originally proposed by Gustensen et al. [34]. In this work, the color model was implemented as described by McClure et al. [47]. Separate LB equations (LBEs) were used to track mass transport for each fluid and the total momentum. Two discrete velocity sets for two phase flows are considered, in which momentum transport LBEs rely on a 3D, 19 discrete velocity (D3Q19) lattice structure and the mass transport LBEs rely on a 3D, seven discrete velocity (D3Q7) lattice structure. In the D3Q19 lattice structure, the lattice velocity vectors corresponding to direction *q*, where *q*=0,1,2,…18, is defined as:

$\boldsymbol{e}_0$ =(0,0,0), $\boldsymbol{e}_1$ =(1,0,0)c, $\boldsymbol{e}_2$ =(-1,0,0)c

$\boldsymbol{e}_3$ =(0,1,0)c, $\boldsymbol{e}_4$ =(0,-1,0)c, $\boldsymbol{e}_5$ =(0,0,1)c, $\boldsymbol{e}_6$ =(0,0,-1)c

$\boldsymbol{e}_7$ =(1,1,0)c, $\boldsymbol{e}_8$ =(-1,1,0)c, $\boldsymbol{e}_9$ =(1,-1,0)c, $\boldsymbol{e}_{10}$ =(-1,-1,0)c

$\boldsymbol{e}_{11}$ =(0,1,1)c, $\boldsymbol{e}_{12}$ =(0,-1,1)c, $\boldsymbol{e}_{13}$ =(0,1,-1)c, $\boldsymbol{e}_{14}$ =(0,-1,-1)c

$\boldsymbol{e}_{15}$ =(1,0,1)c, $\boldsymbol{e}_{16}$ =(-1,0,1)c, $\boldsymbol{e}_{17}$ =(1,0,-1)c, $\boldsymbol{e}_{18}$ =(-1,0,-1)c

where $c = \Delta x / \Delta t$, in which Δx is the lattice spacing and Δt is the time step. In the D3Q7 lattice structure, the velocity vectors match the first seven discrete velocities in the D3Q19 lattice structure.

The mass transport LBEs provide a solution for the densities of the two fluids, ρ_w and ρ_n, which provide the position of the two fluids and the location of the interface between them. The phase indicator field can consequently be computed from the fluid densities as

$$\varphi = \left(\rho_n - \rho_w\right) / \left(\rho_n + \rho_w\right) \tag{2}$$

The value of the phase indicator field is constant within the pure phase regions occupied by each fluid, and varies between -1 and 1 in the interfacial region, which is diffuse. Based on this information, stresses that arise within the interfacial region (as a consequence of the interfacial tension) are incorporated into the momentum transport equation. The color gradient is defined as:

$$\mathbf{C} = \nabla \varphi \tag{3}$$

In the LB formulation the color gradient is re-expressed in terms of its magnitude $|C|$ and normal direction $\mathbf{n} = \mathbf{C} / |\mathbf{C}|$. The D3Q7 mass transport distributions are initialized for each of the two components based on the associated densities and the fluid velocity to match an equilibrium distribution where the flux of mass across the interface is minimized for each fluid:

$$g_{nq} = \omega_q \left[\rho_n \left(1 + \mathbf{e}_q \cdot \mathbf{u}\right) + \beta \left(\mathbf{e}_q \cdot \mathbf{n}\right) \rho_w \rho_n / (\rho_w + \rho_n) \right] \tag{4}$$

$$g_{wq} = \omega_q \left[\rho_w \left(1 + \mathbf{e}_q \cdot \mathbf{u}\right) - \beta \left(\mathbf{e}_q \cdot \mathbf{n}\right) \rho_w \rho_n / (\rho_w + \rho_n) \right] \tag{5}$$

where β is a parameter that controls the width of the interface and **u** is the flow velocity (determined from the momentum transport LBE described below). The associated weights for the D3Q7 model are $\omega_0 = 1/3$ and $\omega_{1\ldots6} = 1/9$. The time evolution of fluid densities is then determined by applying a streaming step directly to the equilibrium distributions (with no relaxation process):

$$\rho_i \left(\mathbf{x}, t + \Delta t\right) = \sum_q g_{iq} \left(\mathbf{x} - \mathbf{e}_q \Delta t, t\right) \qquad (i=w,n) \tag{6}$$

The mass transport LBEs exactly conserve the mass of each component.

The momentum transport is described by a D3Q19 MRT LBE:

$$f_q(\mathbf{x} + \mathbf{e}_q \Delta t, t + \Delta t) - f_q(\mathbf{x}, t) = M^*_{qi} \Lambda_i \left(m_i^{eq} - m_i\right) \tag{7}$$

where q=0,1,2,…18, i=0,1,2,…18; f_q(**x**,t) is the particle-distribution function specifying the probability that fluid particles at lattice location **x** and time t travel along the q^{th} direction, known as collision step; $f_q(\mathbf{x} + \mathbf{e}_q \Delta t, t + \Delta t)$ is streaming step moves distributions between adjacent lattice sites. In the MRT formulation, a relaxation process is applied to a set of nineteen moments determined from the distributions, with the rate of the relaxation process determined by Λ_i. The

relaxation rates are chosen to specify the fluid viscosity [51]. The moments are obtained from a linear transformation, $m_i = M_{iq} f_q$. The matrix M^*_{qi} is the inverse of M_{iq}. The equilibrium moments m_i^{eq} depend on the color gradient **C** and the flow velocity **u**. The macroscopic fluid density and velocity are calculated with the following two equations:

$$\rho = \sum_{q=0}^{18} f_q \tag{8}$$

and

$$\mathbf{u} = \frac{\sum_{q=0}^{18} f_q e_q}{\rho} \tag{9}$$

Fluid pressure is calculated using $p = c_s^2 \rho$, where c_s is the speed of sound. In the LB D3Q19 model, $c_s^2 = c^2/3$.

The non-zero equilibrium moments are

$$m_1^{eq} = \left(j_x j_x + j_y j_y + j_z j_z\right) + \alpha |\mathbf{C}| \tag{10}$$

$$m_9^{eq} = \left(2 j_x j_x - j_y j_y - j_z j_z\right) + \alpha |\mathbf{C}| \left(2 n_x n_x - n_y n_y - n_z n_z\right)/2 \tag{11}$$

$$m_{11}^{eq} = \left(j_y j_y - j_z j_z\right) + \alpha |\mathbf{C}| \left(2 n_y n_y - n_z n_z\right)/2 \tag{12}$$

$$m_{13}^{eq} = j_x j_y + \alpha |\mathbf{C}| n_x n_y / 2 \tag{13}$$

$$m_{14}^{eq} = j_y j_z + \alpha |\mathbf{C}| n_y n_z / 2 \tag{14}$$

$$m_{15}^{eq} = j_x j_z + \alpha |\mathbf{C}| n_x n_z / 2 \tag{15}$$

where the parameter α is linearly related to the interfacial tension and the fluid momentum is computed from the distributions

$$\mathbf{j} = \sum_q f_q \mathbf{e}_q \tag{16}$$

The specific forms for **M** and m_i^{eq} have been previously published in the literature, along with details on setting the relaxation rates, Λ_i, and boundary conditions for two-flow in porous media (see [47]). This formulation was used to measure the relative permeability based on steady-state two-fluid flow within 3D images of a digital rock geometry. An in-depth description of the approach used to estimate relative permeability from digital rock images using the color LB method is provided by Ramstad et al. [53]. More details about the LB multiphase flow simulator used in this study can be found in our recent publications [29,30,47].

3. Important dimensionless numbers

In this study, the role of the critical dimensionless numbers on multiphase flows in 3D, complex porous media was investigated. These dimensionless numbers included the contact angle, Ca number, and viscosity ratio.

Wettability plays a significant role in determining multiphase fluid flow and distribution in porous media. It is defined as “the tendency of one fluid to spread on or adhere to a solid surface in the presence of other immiscible fluids” [3]. Wettability can be expressed in a more convenient and precise manner by measuring the angle of contact at the liquid-solid surface. According to

Iglauer et al. [40], a CO_2-brine-rock system is considered completely water-wet for a contact angle of 0°, strongly water-wet for 0°-50°, weakly water-wet for 50°-70°, intermediate wet for 70°-110°, weakly CO_2-wet for 110°-130°, strongly CO_2-wet for 130°-180°, and completely CO_2-wet for a contact angle of 180°. Existing studies showed, with the decrease of the relative adhesion of the wetting fluid to the solid surface at a given wetting fluid saturation, the non-wetting fluid's relative permeability decreases whereas the wetting fluid's relative permeability increases [4,28,42].

In natural geologic reservoir rocks, the wetting fluid preferentially coats the majority of the rock surfaces and tends to be held in the smaller pores. On the other hand, the non-wetting fluid tends to be repelled from the rock surfaces, occupy the center of large pores, and flow in the center of channels. At high Ca numbers, the viscous force dominates the flow and thus the mobility of both fluids increases. Conversely, as the Ca number decreases, two-phase flow might be blocked in some places due to the capillary resistance [13], leading to decreased mobility of both fluids. The Ca number, defined in Equation 17 [53], measures the ratio of the viscous force to the capillary force:

$$Ca = \frac{\mu_{nw} u_t}{\sigma} \tag{17}$$

where μ_{nw} is the non-wetting fluid dynamic viscosity, u_t is the total average Darcy flow velocity, and σ is the interfacial tension between wetting and non-wetting fluids.

The viscosity ratio also has a critical effect on the relative permeability characteristics of a reservoir rock, which is defined as the ratio of the non-wetting fluid viscosity to the wetting fluid viscosity:

$$M = \mu_{nw} / \mu_w \tag{18}$$

where μ_w is the dynamic viscosity of the wetting fluid. When the Ca number is small, the fluid viscosity ratio has little effects on the relative permeability because most of the fluid interfaces are immobilized in narrow throats [13]. Conversely, when the Ca number increases, the relative importance of the viscous force and capillary force changes. In this study, in order to study the dynamic effects of Ca number and viscous ratio on relative permeability curves, two Ca numbers ($Ca = 1\times10^{-4}$ and $Ca = 1\times10^{-3}$) and two viscosity ratios (M=0.25 and M=1) were investigated. For each combination of Ca and M, three contact angles were used in the LB two-phase flow simulation.

A literature review of relevant studies on LB simulations of multiphase flow in porous media was summarized in Table 1. In the table, the computational domain size is measured using the lattice length unit (lu) in LB modeling. Based on this review, there is no pore-scale LB multiphase flow modeling work that studies the comprehensive interactions between all the three dimensionless numbers (contact angle, Ca, and M) in the 3D pore spaces of a real reservoir rock, as well as their role on the larger-scale relative permeability curves in the rock.

Table 1 A literature review and relevant works on multiphase flow

Reference	Material	Dimension	Domain size (lu)	Resolution (μm/lu)	Dimensionless numbers	Relative Permeability Curves
Zhao et al. 2017 [65]	Sandstone	2D	3600 × 1920	N/A[1]	Ca, M, contact angle	Yes
Gu et al. 2018 [35]	Berea Sanstone	2D	2644 × 2117	0.67	M, contact angle	Yes
Ramstad et al. 2010 [52]	Bentheimer Sandstone	3D	256 × 256 × 256	6.67	Ca	Yes
Ramstad et al. 2012 [53]	Bentheimer and Berea sandstone	3D	256 × 256 × 256	6.67	M	Yes
Boek & Venturoli 2010 [15]	Bentheimer and Berea sandstone	3D	128 × 128 × 128	4.9	N/A	Yes
Li et al. 2014 [46]	Sandstone	3D	200 × 200 × 50	3.7	N/A	No
Alpak et al. 2018 [2]	Gildehauser sandstone	3D	512 × 512 × 512	4	N/A	Yes
Landry et al. 2014 [43]	glass bead and polyethylene bead packs	3D	200 × 200 × 200	26	contact angle	Yes
Li et al. 2005 [45]	computer-generated sphere-packed porous media	3D	96 × 96 × 96	N/A	Ca, M, contact angle	Yes
Ghassemi and Pak, 2011 [31]	computer-generated pore structures with solid and void blocks	2D	261 × 261	2×10^4	Ca, M, contact angle	Yes

1. **"**N/A" denotes "not available".

4. Results and Discussion

4.1 Pore-scale contact angle measurement and SEM/EDX characterization

In the LB simulations, the discrete, digitalized rock microstructure was obtained directly from DOE-NETL's 3D micro-CT scanned images of the Berea sandstone sample. The sandstone was scanned in top, middle, and bottom sections separately in order to obtain a larger field of view that can account for spatial heterogeneity. In each section, a computational domain of 800 × 800 × 600 pixels in the x, y, and z directions was reconstructed based on the CT images, where z is the vertical direction. Note that 800 × 800 pixels (in the x-y plane) is the maximum possible dimensions that can be achieved after removing the outer air areas. The lattice spacing is equal to the CT image pixel size, thus the LB model had a resolution of 2.36 μm/lu, the same as the CT image resolution. The distance from the bottom face of the top computational domain to the top face of the middle

computational domain was 0.354 mm, and the distance from the bottom face of the middle computational domain to the top face of the bottom computational domain was 1.345 mm, as illustrated in **Fig. 2**. Pore-scale contact angles were measured quantitatively using image processing methods throughout all the three computational domains based on NETL's 3D micro-CT reconstructions, and the distribution curve is illustrated in **Fig. 3**. Specifically, the frequency of each contact angle was counted directly in the 3D micro-CT image reconstructions and then normalized by the total number of measured contact angles. Pore-scale contact angle measurements showed that the contact angles had a minimum value of 8.6°, a maximum value of 104.3°, a mean value of 46.2°, and a median value of 45.4°. The mean and median contact angles fell in the range of 0°-50°, which is strongly water-wet based on the definition of Iglauer et al. [40]. The relatively wide range between the minimum and maximum contact angles suggests heterogeneous rock surface wettability. The variation in rock surface wettability results from heterogeneous surface mineralogy and roughness. In order to confirm this hypothesis, we used the facilities of scanning electron microscope/energy-dispersive X-ray spectroscopy (SEM/EDX) housed in Virginia Tech's Nanoscale Characterization and Fabrication Laboratory to characterize the Berea sandstone's surface roughness and mineralogy. **Fig. 4** demonstrates the results of the SEM/EDX characterization. Specifically, Figures 4a and 4b illustrate rock surfaces rich in clay and quartz minerals, respectively, and both of them demonstrate high surface roughness. The areas marked by yellow rectangles were analyzed using EDX, and it was conformed that sample surface in Figure 4a was rich in clay whereas the sample surface in Figure 4b was rich in quartz. In fact, a significant portion of rock surfaces rich in various clay minerals were observed in this particular sandstone sample. These observations explain the relatively wide range of contact angle distribution as illustrated in Fig. 3.

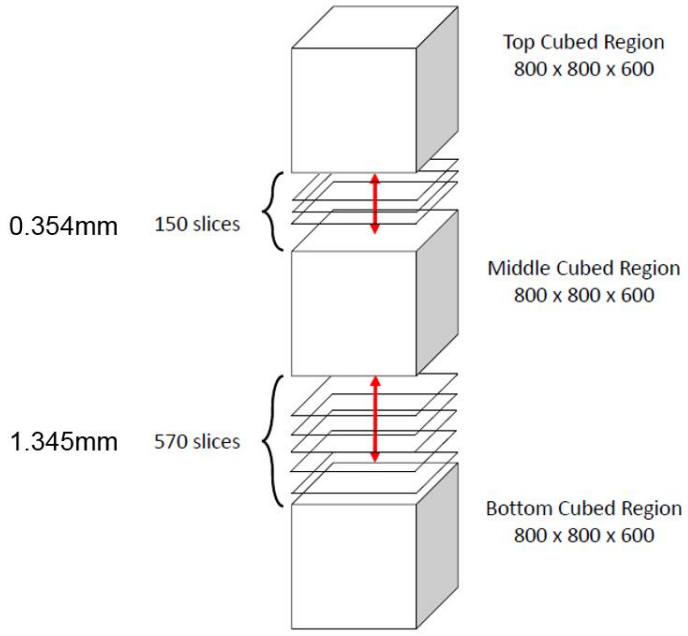

Fig. 2. Schematic plot of the spatial positions of the three computational domains.

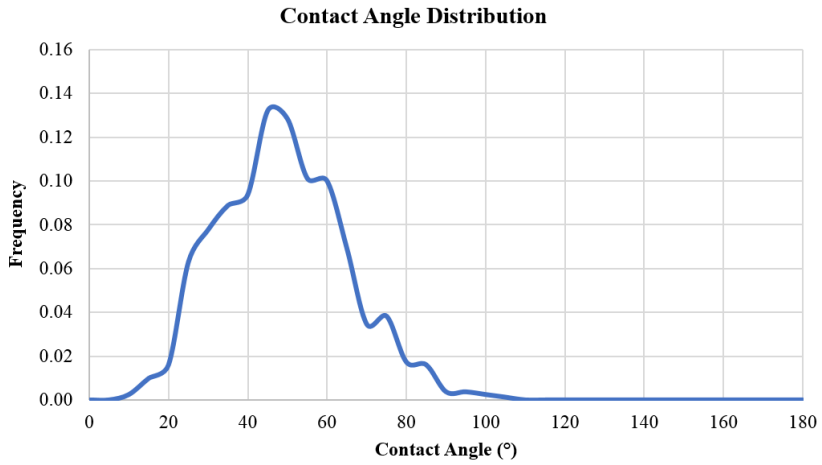

Fig. 3. Contact angle distribution at the pore scale measured directly from NETL's 3D micro-CT image reconstructions.

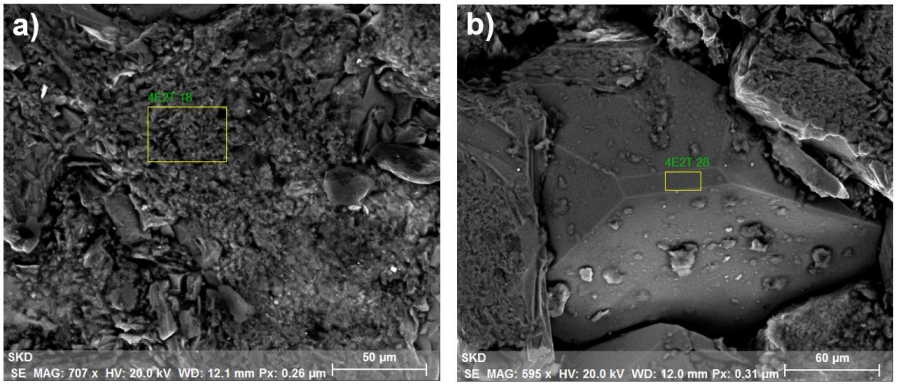

Fig. 4. SEM/EDX characterization of sandstone surface rich in a) clay minerals, and b) quartz.

4.2 Comparison between CT-scanned and LB-simulated water/CO_2 distributions

Fig. 5 illustrates the comparison between micro-CT-scanned and LB-simulated images of CO_2 and water distributions in the pore space of the Berea sandstone. The sandstone pore structure was from the middle-section computational domain. Viscosity ratio was 1:4, Ca number was 1×10^{-4}, and the contact angle was equal to 45°. Figure 5a is the X-ray CT scanned two-fluid distribution in the sandstone whereas Figure 5b is the corresponding LB-simulated two-fluid distribution. The picture is a 2D cross section perpendicular to the main-flow (z) direction and has dimensions of 1.89 mm × 1.89 mm (800 lu × 800 lu). The water is blue, CO_2 is pink, and sandstone is white. In this study, we refer to water and CO_2 as the wetting and non-wetting fluids, respectively. In the LB multiphase flow simulations, fluid phases were initialized morphologically, based on an operation known as morphological opening [29,63], in order to achieve a range of fluid saturations. The CO_2 was instantiated into the larger pores, consistent with water-wet porous media. Multiphase fluid flow was induced by applying a constant external body force with full periodic boundary conditions to mimic fractional flow experiments typically used to measure relative permeability in the laboratory [5,6,53]. In this way, we managed to simulate steady-state two-phase flows through the rock sample in the imbibition process [29], which was consistent with the fluid distribution in the CT scanning stage. Comparison between micro-CT-scanned and LB-

simulated two-fluid distributions showed an overall good agreement that CO_2 was trapped in the center of larger pores, primarily due to the imbibition process associated with relatively low Ca numbers in the laboratory experiment and LB multiphase flow simulation.

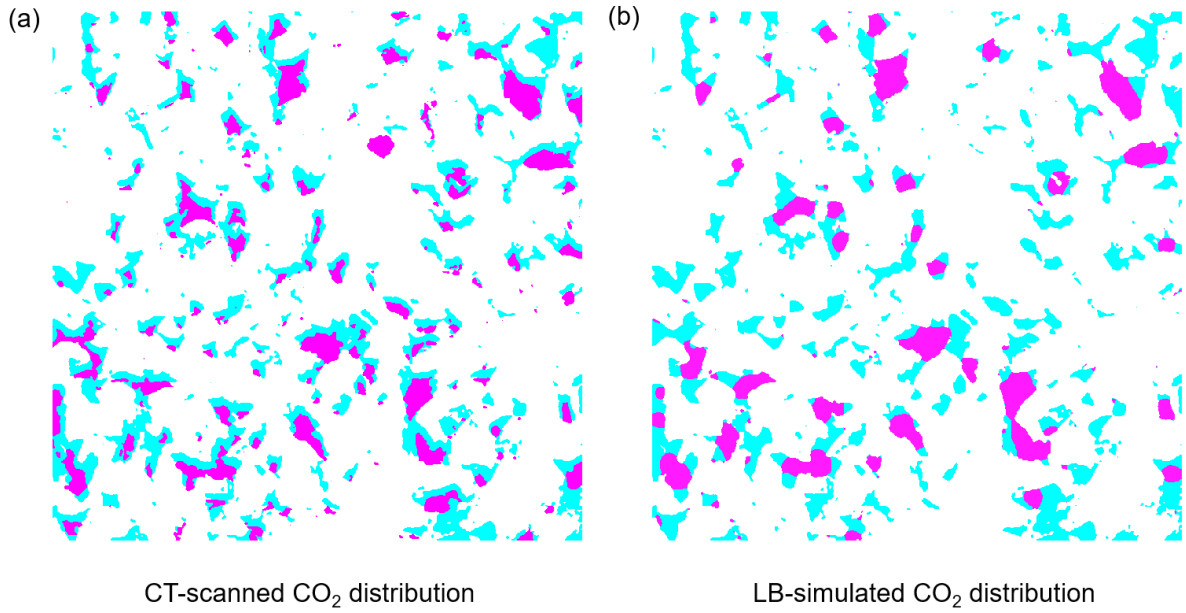

Fig. 5. a) CT scanning image of two-fluid distribution in the sandstone at the pore scale, and b) corresponding LB-simulated two-fluid distribution at the pore scale. The water is blue, CO_2 is pink, and sandstone is white. The pore geometry was a 2D horizontal cross section cut from the 3D X-ray CT image reconstruction of the middle-section computational domain. This cross section is perpendicular to the main-flow (z) direction and has dimensions of 1.89 mm × 1.89 mm (800 lu ×800 lu). The distance from the 2D cross section to the bottom of the computational domain is 0.8 mm.

4.3 Comprehensive sensitivity analyses for various combinations of dimensionless numbers

With the range of contact angles determined at the pore scale based on micro-CT scanning and the LB multiphase flow model calibrated by comparing CT-scanned and LB-simulated two-fluid distributions, we conducted comprehensive sensitivity analyses for various combinations of the dimensionless numbers. The simulation information is summarized in Table 2. In this study, two viscosity ratios (1:4 and 1:1) and two Ca numbers (10^{-3} and 10^{-4}), associated with three contact angles (0, 45, and 90 degrees), were investigated in the middle section sample. The three selected contact angles covered the majority of the contact angle range demonstrated in Fig. 3. Comprehensive combinations between these dimensionless numbers led to twelve scenarios in the LB multiphase flow simulations conducted on the middle-section computational domain, as illustrated in Table 2.

Table 2. Twelve scenarios were considered in the two-phase LB flow simulations, based on comprehensive combinations between the three dimensionless numbers (M, Ca, and contact angle).

Viscosity ratio between CO_2 and water (M)	Ca = 1×10^{-3}		Ca = 1×10^{-4}	
1:4 (0.25)	Contact angle	0°	Contact angle	0°
		45°		45°
		90°		90°
1:1 (1)	Contact angle	0°	Contact angle	0°
		45°		45°
		90°		90°

Fig. 6 demonstrates the role of different combinations of Ca number, viscosity ratio, and contact angle on the relative permeability curves, based on the LB multiphase flow simulations conducted on the middle section of the Berea sandstone sample. Specifically, Figures 6a and 6b have viscosity ratios of 1:1 and 1:4, respectively, with the Ca number fixed at 1×10^{-4}; Figures 6c and 6d have viscosity ratios of 1:1 and 1:4, respectively, with the Ca number fixed at 1×10^{-3}. For each combination of the Ca number and viscosity ratio, contact angles of 0°, 45°, and 90° were simulated, leading to twelve scenarios as demonstrated in Table 2. Based on simulated data, Corey model was used to fit the simulated relative permeability curves. Corey model is an often used approximation of relative permeability, which is a power law based on the normalized water saturation. If S_{wir} is the irreducible saturation of water, S_{orw} is the residual saturation of CO_2 after water flooding, the normalized water saturation is defined in Equation 19:

$$S_w^* = \frac{S_w - S_{wir}}{1 - S_{wir} - S_{orw}} \tag{19}$$

The Corey models for fitting the relative permeability curves of water and CO_2 are then illustrated in Equations 20 and 21:

$$k_{rw} = k_{rw}^o S_w^{*N_w} \tag{20}$$

$$k_{ro} = k_{ro}^o (1 - S_w^*)^{N_o} \tag{21}$$

where k_{rw} is the relative permeability of water; k_{ro} is the relative permeability of CO_2; k_{rw}^o is the maximum relative permeability for water when $S_w^*=1$; k_{ro}^o is the maximum relative permeability for CO_2 when $S_w^*=0$; N_w is the power-law exponent for the water curve; and N_o is the power-law exponent for the CO_2 curve. The fitted Corey model parameters are listed in Tables 3 and 4.

Table 3. Corey model parameters with Ca=1×10^{-4}

Ca 1×10^{-4}	Contact angle	S_{wir}	S_{orw}	N_w	N_o	k_{rw}^o	k_{ro}^o
Viscosity ratio 1:1	0°	0.2	0.05	3.035	2.919	0.97	0.85
	45°	0.15	0.07	3.414	2.782	0.98	0.9
	90°	0.1	0.08	3.455	3.091	0.99	0.85
Viscosity ratio 1:4	0°	0.25	0.07	3.201	4.879	0.81	0.49
	45°	0.2	0.08	3.177	3.803	0.8	0.606
	90°	0.15	0.09	2.552	4.199	0.79	0.61

Table4. Corey model parameters with Ca=1×10^{-3}

Ca 1×10^{-3}	Contact angle	S_{wir}	S_{orw}	N_w	N_o	k_{rw}^o	k_{ro}^o
Viscosity ratio 1:1	0°	0.2	0.04	2.513	1.047	0.99	0.876
	45°	0.15	0.06	2.45	0.987	0.91	0.89
	90°	0.1	0.07	2.172	1.159	0.93	0.893
Viscosity ratio 1:4	0°	0.23	0.05	2.508	1.641	0.8	0.58
	45°	0.19	0.07	2.362	1.583	0.75	0.66
	90°	0.14	0.08	1.878	1.694	0.81	0.75

4.4 Effect of contact angle

The contact angle is one of the most important dimensionless numbers in two-phase displacement through a porous media, and its effect was studied at 0°, 45°, and 90°. From Fig. 6, it is observed that when the contact angle decreased both the wetting (water) and non-wetting (CO_2) fluid relative permeability curves moved to the right, which implies that the wetting fluid relative permeability decreased whereas the non-wetting fluid relative permeability increased. In addition, Corey model fitting showed that S_{wir} increased whereas S_{orw} decreased when contact angle decreased continuously, as illustrated in Tables 3 and 4. In this water-wet sandstone, the wetting fluid tends to coat the rock surfaces to form a thin water film and occupies most of the small pores. A decreasing contact angle led to an increasing affinity between water and the solid surfaces which pushed water toward the rock surfaces and thus led to higher resistance and lower relative permeability for water. Furthermore, because the capillary pressure increased with the decreasing contact angle, it took more energy for the wetting fluid to move and it might be trapped in small pores, which reduced the overall connectivity and consequently the relative permeability of the wetting fluid. On the other hand, because the non-wetting fluid occupies larger pores and flows in the center of flow channels, a decreasing contact angle will push the wetting fluid toward the solid surfaces and thus reduce its competition with the non-wetting fluid flow; this process is favorable to the overall flow rate of the non-wetting fluid, leading to the increase of non-wetting fluid relative permeability. Similar results have been observed through experiments conducted by Donaldson and Thomas [28] and reported by Li et al. [45] and Ghassemi and Pak [31] through numerical simulations. It is also interesting to notice that at the contact angle of 90°, both wetting and non-wetting fluid relative permeability curves are far away from the other curves (i.e., the 0° and 45°

curves). This geometric effect can be attributed to special fluid configurations at this angle, with which both fluids have less affinity to the rock surfaces.

4.5 Effect of viscosity ratio

To investigate the effect of viscosity ratio on relative permeability curves, two viscosity ratios (M=1:1 and M=1:4) were considered in the LB multiphase flow simulations. Specifically, a viscosity ratio of 1:4 between CO_2 and water is typical of $scCO_2$ injection in deep saline aquifers [19,20]. As discussed previously, when the Ca number is fixed, a decreasing contact angle (i.e., increasing affinity between water and rock surfaces) caused both water and CO_2 relative permeability curves to move to the right, implying that the water relative permeability decreases whereas the CO_2 relative permeability increases under the impact of the decreasing contact angle. In the case of $Ca = 10^{-4}$ and with a continuously decreasing contact angle, increasing the viscosity ratio from 1:4 (see Fig. 6b) to 1:1 (see Fig. 6a) facilitates the increase of CO_2 relative permeability (i.e., the distance between the three CO_2 relative permeability curves becomes larger) while mitigating the reduction of water relative permeability (i.e., the distance between the three water relative permeability curves becomes smaller). This is because the wetting fluid tends to coat the solid surfaces as a thin film whereas the non-wetting fluid tends to occupy larger pores and thus experiences a hydraulic slip at the two-phase interface, which is well known as the lubrication effect [12,27,31,39,45,48,64]. Increasing the viscosity ratio has the potential to enhance the lubrication effect [39,45], because the thin wetting fluid layer, which is located between the non-wetting fluid and rock surfaces, becomes less viscous relative to the non-wetting fluid and thus enables the non-wetting fluid to flow more easily. In the meanwhile, when the viscosity ratio increases the wetting fluid becomes less viscous relative to the non-wetting fluid, which is also favorable for the mobility of the wetting fluid and thus mitigates the reduction of the wetting fluid relative permeability under the impact of a decreasing contact angle. Similar phenomena can be observed in the case of $Ca = 10^{-3}$ (see Figures 6c and 6d). Based on these observations, it is clear that the viscosity ratio affects the rate of change of the relative permeability curves for both wetting and non-wetting fluids, when the contact angle varies continuously.

In the literature, most works studied the role of viscosity ratio when the contact angle was fixed. Several groups reported that a larger viscosity ratio enhances the non-wetting fluid relative permeability whereas the wetting fluid relative permeability is relatively insensitive to the change of viscosity ratio at a fixed contact angle [7,8,27,31,39,45]. In contrast, the primary novel finding in this paper is that the viscosity ratio affects the rate of change of the relative permeability for both phases when the contact angle changes continuously. This new finding is critical and has important implications to geologic CO_2 storage, because natural reservoir rocks have heterogeneous contact angles at the pore scale. As a consequence, the dependence of relative permeability curves on the viscosity ratio will be complicated due to the heterogeneous contact angles.

4.6 Effect of Ca number

In the LB simulations, the Ca number was adjusted by changing the external body force with all the other parameters fixed. In Fig. 6, it is observed, at a fixed wetting fluid saturation and under the same viscosity ratio, both wetting and non-wetting fluid relative permeabilities increased with the increasing Ca number (e.g., comparing Figures 6a with 6c, or comparing Figures 6b with 6d). In addition, Fig. 6 illustrates that the curvature of the relative permeability curves under $Ca=10^{-3}$ was lower than that under $Ca=10^{-4}$, which suggests that the relative permeability curves under

$Ca=10^{-3}$ were straighter. This is consistent with the finding that the values of N_o and N_w under $Ca=10^{-3}$ are significantly lower than those under $Ca=10^{-4}$, as shown in Tables 3 and 4. This is because an increasing Ca number enhances the inertial force relative to the capillary force, which helps both wetting and non-wetting fluids to overcome the capillary resistance and to form more well-connected flow pathways, leading to increased mobility and relative permeability for both fluids.

To summarize, in this study it is the first time that LB multiphase flow simulation is used to demonstrate the comprehensive interactions between contact angle, viscosity ratio, and Ca number, as well as their role on the relative permeability curves within a complex, 3D sandstone sample, of which the pore structural information is directly obtained by non-invasive X-ray micro-CT imaging. Our comprehensive sensitivity analyses illustrated that the impact of the changing contact angle on relative permeability curves depends primarily on both the viscosity ratio and Ca number. In the literature, most works studied the role of viscosity ratio when the contact angle was fixed. Conversely, this study shows that the viscosity ratio affects the rate of change of the relative permeability for both fluids when the contact angle changes continuously. Simulation results are consistent with fundamental multiphase flow physics and imply that these critical dimensionless numbers, which are associated with water/CO_2 multiphase flows with respect to geologic carbon storage, are interconnected and must be studied in a holistic manner.

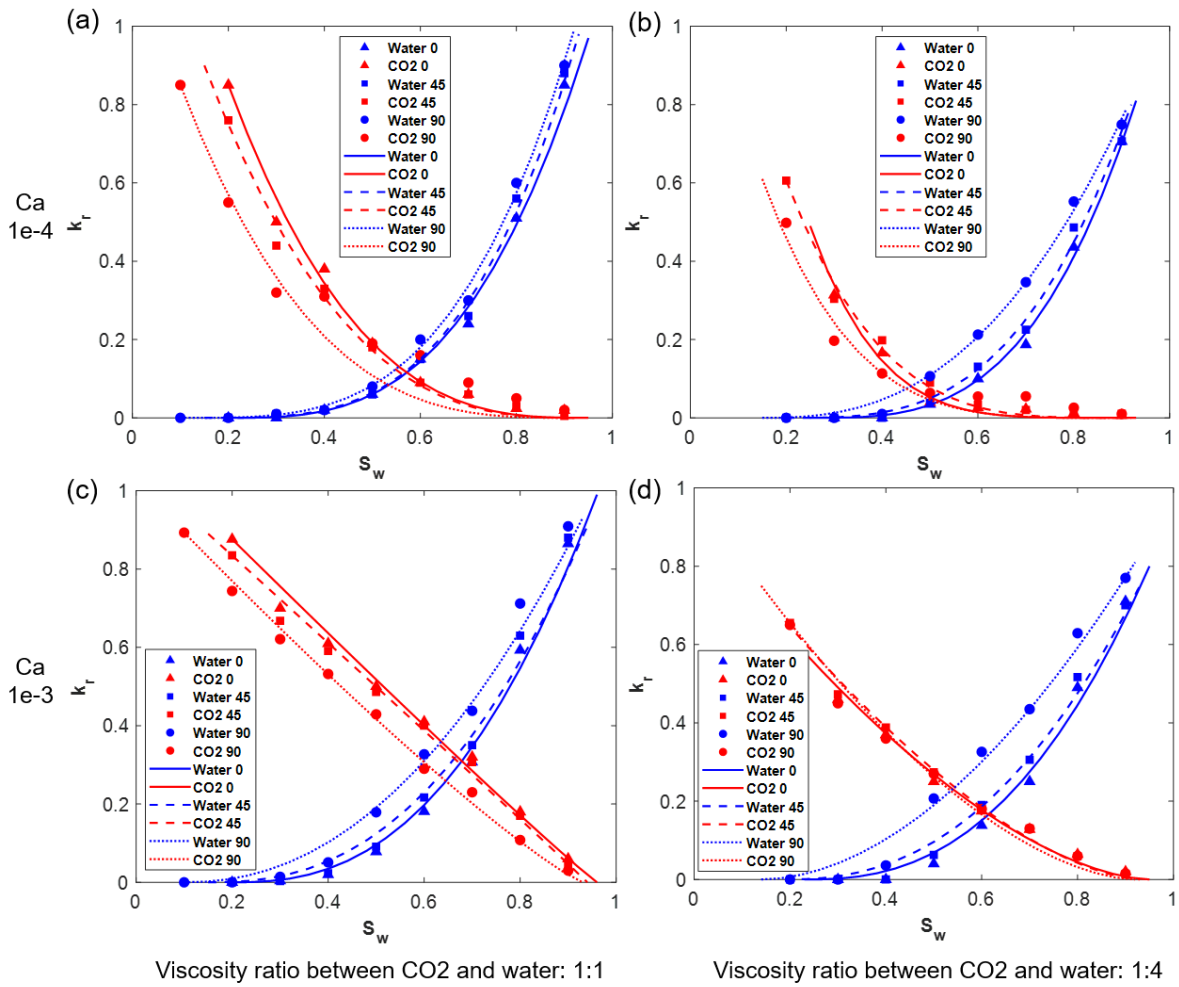

Fig. 6. Relative permeability vs. water saturation (S_w) curves under two Ca numbers ($Ca=1\times10^{-4}$ and $Ca=1\times10^{-3}$) and two viscosity ratios (M=0.25 and M=1). The data points are LB-simulated relative permeabilities and the curves are from Corey model fitting. Contact angles of 0°, 45°, and 90° were simulated for each combination of Ca number and viscosity ratio. The computational domain was the middle section of the Berea sandstone sample.

4.7 Effect of anisotropy and spatial heterogeneity

In previous numerical simulations, fluid flow was in the z direction (upward). In order to study the effect of flow direction anisotropy, we ran a LB simulation with flow in the –z direction (downward). Both LB simulations (upward and downward flow directions) were conducted on the middle-section Berea sandstone with $Ca=1\times10^{-4}$, M=0.25, and contact angle θ = 0°, 45°, and 90°. From **Fig. 7a** and **7b**, it is observed that the relative permeability curves are slightly different between the two flow directions. Because the flow paths are heterogeneous, flipping the flow direction changes the final non-wetting fluid configuration in the 3D pore space even when all the other flow conditions are the same. This affects both the wetting and non-wetting fluid relative permeabilities measured in the final, steady state. The implication from this simulation is that multiphase fluid configurations assume different geometries in the 3D pore space depending on the flow direction.

On the same middle-section Berea sandstone sample and with the same Ca number and viscosity ratio, we simulated the multiphase flow scenario with flow in the x (horizontal) direction, as shown in **Fig. 7c**. By comparing Fig. 7a and Fig. 7c, it can be found that the relative permeability curves for both fluids changed and the change in the non-wetting fluid relative permeability curves was larger after the flow direction was switched to the x direction. As discussed previously, the non-wetting fluid tends to occupy larger pore networks and to flow in the middle of channels, whereas the wetting fluid tends to occupy smaller pore networks and to flow near rock surfaces. The fact that the non-wetting fluid relative permeability experienced a more significant change after flow direction switch implies that the larger pore networks demonstrate stronger anisotropy (difference of flow path connectivity between the x and z directions) compared to the smaller pore networks. This is reasonable because the number of larger pores is much less than that of smaller pores in sedimentary rocks [16,18], leading to stronger anisotropic effects in the larger pore networks in terms of pore throat size and pore space connectivity, which consequently affects the relative permeability of the non-wetting fluid to a more noticeable extent.

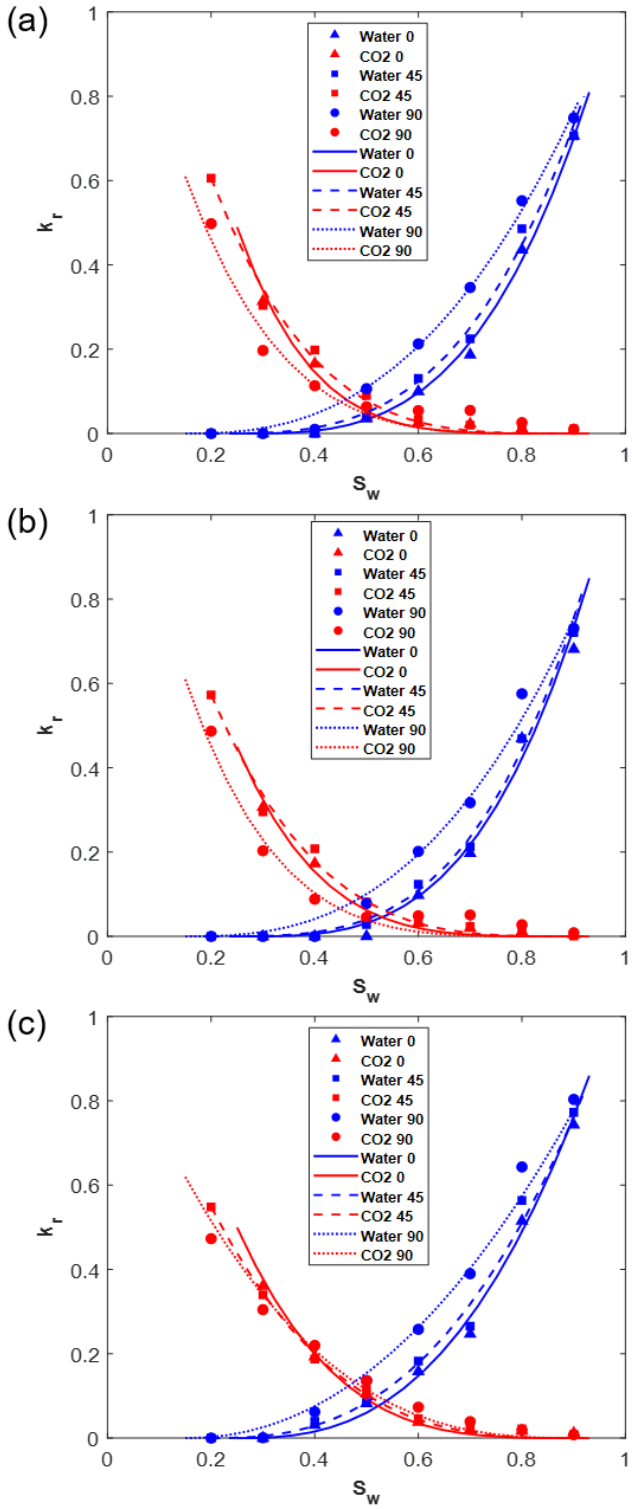

Fig. 7. Relative permeability vs. wetting fluid saturation (S_w) curves for fluid injection directions (a) from bottom to top in the z direction, (b) from top to bottom in the –z direction, and (c) in the horizontal (x) direction. The simulations were conducted on the middle-section computational domain with $Ca=1\times10^{-4}$ and M=0.25. The data points are LB-simulated relative permeabilities and the curves are from Corey model fitting.

We also conducted LB multiphase flow simulations in the top- and bottom-section computational domains, with Ca=1×10^{-4} and M=1. The flow direction was upward in the z (vertical) direction in both computational domains. The distance between top section center and bottom section center is 4.53 mm. **Fig. 8** illustrates that there were noticeable changes in both the wetting and non-wetting fluid relative permeability curves, which implies that pore geometry heterogeneity can be observed even over such a small distance. Therefore, special attention should be paid to these micro-scale heterogeneities for relative permeability analysis. Moreover, insight gained from the studies of small-scale heterogeneity will benefit the understanding of relative permeability upscaling in geologic formations.

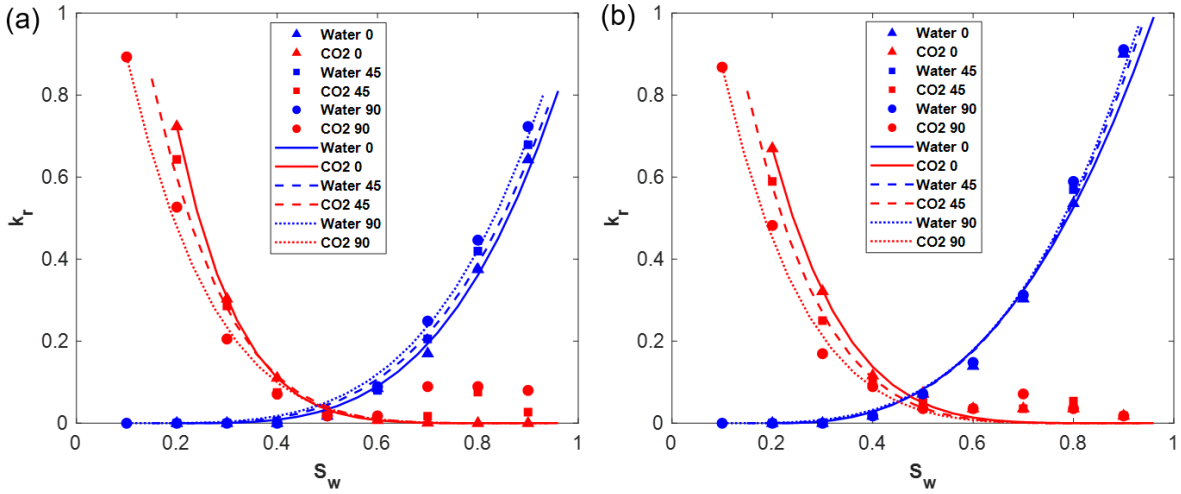

Fig. 8. Relative permeability vs. wetting fluid saturation (S_w) curves in the (a) top-section, and (b) bottom-section computational domains. In the simulations, Ca=1×10^{-4} and M=1. The data points are LB-simulated relative permeabilities and the curves are from Corey model fitting.

5. Conclusions

The main focus of this research is on the dependence of relative permeability curves on the contact angle, Ca number, viscosity ratio, as well as the various combinations between them. The influence of anisotropy and micro-scale spatial heterogeneity of the rock sample on the relative permeability curves was also studied. The LB-simulated water/CO_2 distribution agreed well with the micro-CT-scanned water/CO_2 distribution, which validated the capability of the LB method in simulating multiphase flow in complex, 3D porous media. Simulation results showed that a decreasing contact angle causes a decrease in wetting fluid relative permeability and an increase in non-wetting fluid relative permeability. A rising Ca number increases both wetting and non-wetting fluid relative permeabilities, because the higher inertial force favors the mobility of both fluids. An increasing viscosity ratio facilitates the increase of non-wetting fluid relative permeability and mitigates the reduction of wetting fluid relative permeability, when the contact angle decreases continuously. This is because the lubrication effect is stronger when the wetting fluid viscosity is reduced, leading to enhanced non-wetting fluid relative permeability. The reduced wetting phase viscosity is also favorable for the mobility of the wetting fluid, which mitigates the decrease of the wetting fluid relative permeability when the contact angle decreases continuously. These phenomena demonstrated that the role of the changing contact angle on relative permeability curves depends primarily on both the viscosity ratio and Ca number.

In the literature, most works studied the role of viscosity ratio when the contact angle was fixed. Several groups reported that a larger viscosity ratio enhances the non-wetting fluid relative permeability whereas the wetting fluid relative permeability is relatively insensitive to the change of viscosity ratio at a fixed contact angle. In contrast, the primary novel finding of this study is that the viscosity ratio affects the rate of change of the relative permeability for both phases when the contact angle changes continuously. This new finding is critical and has significant implications to geologic CO_2 storage because natural reservoir rocks have heterogeneous contact angles at the pore scale. To the best of our knowledge, it is the first time that comprehensive interactions between these dimensionless numbers are demonstrated in a real 3D sandstone sample using LB multiphase flow simulations. The simulation results are consistent with fundamental multiphase flow physics and imply that these critical dimensionless numbers, which are associated with water/CO_2 multiphase flows with respect to geologic carbon storage, are interconnected and must be studied in a holistic manner. We also investigated the role of the changes of fluid injection direction and sample location on relative permeability curves. Simulation results showed that the change in non-wetting fluid relative permeability was larger when the flow direction was switched from vertical to horizontal, which indicated that there was stronger anisotropy in larger pore networks that tended to be occupied by the non-wetting fluid.

The well-controlled core flooding and X-ray micro-CT experiments provided accurate pore structural information and pore-scale contact angle measurements as inputs for the LB multiphase flow model. The combination of micro-CT imaging and LB multiphase flow simulation is a promising tool for advancing fundamental understanding of the interactions between the critical dimensionless numbers that regulate multiphase flow in complicated 3D pore space. Moreover, this study has the potential to advance fundamental understanding of the multiphysics processes associated with multiphase flow in geologic materials, which provides insight into upscaling methodologies that aim to account for the influence of pore-scale processes in core- and larger-scale modeling frameworks.

Acknowledgements

The authors acknowledge the support of the Junior Faculty Award from Virginia Tech's Institute for Critical Technology and Applied Science and the computational resources from Virginia Tech's Advanced Research Computing Center. The authors are also thankful to the support from the National Energy Technology Laboratory Research Participation Program, sponsored by the U.S. Department of Energy and administered by the Oak Ridge Institute for Science and Education.

Nomenclature

c: Lattice speed

c_s: Speed of sound

$\boldsymbol{C}$: Color gradient

Ca: Capillary number

$\boldsymbol{e}_q$: Lattice velocity vector

f_q : Particle-distribution function

$\mathbf{g}$: Gravity vector

g_{iq} : Mass transport distribution

$\boldsymbol{j}$: Fluid momentum

$\boldsymbol{k}$: Permeability tensor

k_{ri} : Relative permeability

k_{rw} : Wetting phase relative permeability

k_{ro} : Non-wetting phase relative permeability

k_{rw}^{o} : End point of wetting phase saturation

k_{ro}^{o} : End point of non-wetting phase saturation

M_{iq} : Transformation matrix

M_{qi}^{*} : Inverse of M_{iq}

m_i^{eq} : Equilibrium moments

M : Viscosity ratio

$\boldsymbol{n}$: Unit normal vector of the color gradient

N_w : Corey wetting phase exponent

N_o : Corey non-wetting phase exponent

P : Fluid pressure

∇p : Pressure gradient

ρ_i : Density

S_{wir} : Irreducible saturation of wetting phase

S_{orw} : Residual saturation of non-wetting phase after wetting phase flooding

S_w: Wetting phase saturation

S_w^*: Normalized wetting phase saturation

$\boldsymbol{t}$: Time

Δt: Time step

$\boldsymbol{u}$: Flow velocity

v_i: Darcy velocity

u_t: Total average Darcy flow velocity

μ_{nw}: Dynamic viscosity of the non-wetting fluid

μ_w: Dynamic viscosity of the wetting fluid

μ_i: Dynamic viscosity

ω_q: Weights for D3Q7 model

Δx: Lattice spacing

$\boldsymbol{x}$: Location

φ: Phase field indicator

Λ_i: Rate of the relaxation process

α: A parameter that linearly related to the interfacial tension

β: A parameter that controls the width of the interface

σ: Interfacial tension between wetting and non-wetting fluids

Reference

[1] Aggelopoulos, C.A. and Tsakiroglou, C.D. 2008. The Effect of Micro-heterogeneity and Capillary Number on Capillary Pressure and Relative Permeability Curves of Soils. Geoderma. 148: 25–34

[2] Alpak, F.O., Berg, S., and Zacharoudiou, I. 2018. Prediction of Fluid Topology and Relative Permeability in Imbibition in Sandstone Rock by Direct Numerical Simulation. Advances in Water Resources, 122: 49-59

[3] Anderson, W. G. 1986. Wettability Literature Survey—Part 1, Rock/Oil/Brine Interactions and the Effects of Core Handling on Wettability. Journal of Petroleum Technology. 38: 1125–1144
[4] Anderson, W. G. 1987. Wettability Literature Survey—Part 5: The Effects of Wettability on Relative Permeability, Journal of Petroleum Technology. 39(11): 1453–1468
[5] Armstrong, R T., McClure, J. E., Berrill, M. A. et al. 2016. Beyond Darcy's Law: The Role of Phase Topology and Ganglion Dynamics for Two-fluid Flow. Physical Review E 94 (4): 043113. https://doi.org/10.1103/PhysReveE.94.043113.
[6] Armstrong, R. T., McClure, J. E., Berill, M. A. et al. 2017. Flow Regimes During Immiscible Displacement. Petrophysics 58 (1): 10–18. SPWLA-2017-v58n1a1.
[7] Avraam, D.G. and Payatakes, A.C. 1995a. Generalized Relative Permeability Coefficients during Steady-state Two-phase flow in Porous Media and Correlation with the Flow Mechanisms. Transp. Porous Media 20: 135–168
[8] Avraam, D.G. and Payatakes, A.C. 1995b. Flow Regimes and Relative Permeabilities during Steady-state Two-phase Flow in Porous Media. J. Fluid Mech. 293: 207–236
[9] Avraam, D.G. and Payatakes, A.C. 1999. Flow Mechanisms, Relative Permeability, and Coupling Effects in Steady-state Two-phase Flow Through Porous Media. The Case of Strong Wettability. Ind. Eng. Chem. Res. 38: 778–786
[10] Bernaschi, M., Fatica, M., Melchionna, S., Succi, S., and Kaxiras, E. 2010. A Flexible High Performance Lattice Boltzmann GPU Code for the Simulations of Fluid Flows in Complex Geometries. Concurrency Comput. Pract. Exp. 22: 1–14
[11] Blunt, M.J., Bijeljic, B., Dong, H., Gharbi, O., Iglauer, S., Mostaghimi, P., Paluszny, A., Pentland, and C.H. 2013. Pore-scale Imaging and Modelling. Advances in Water Resources. 51: 197–216, http://dx.doi.org/10.1016/j.advwatres.2012.03.003.
[12] Blunt, M.J., King, M.J., and Scher, H. 1992. Simulation and Theory of Two-phase Flow in Porous Media. Phys. Rev. A 46: 7680–7699
[13] Blunt M.J. and King P. 1991. Relative Permeabilities from Two- and Three Dimensional Pore-scale Network Modelling. Transport Porous Med. 6:407–33
[14] Blunt, M.J., Jackson M.D., Piri, M., and Valvatne, P.H. 2002. Detailed Physics, Predictive Capabilities and Macroscopic Consequences for Pore-network Models of Multiphase Flow. Adv Water Resources. 25:1069–89
[15] Boek, E.S., Venturoli, M., 2010. Lattice-Boltzmann Studies of Fluid Flow in Porous Media with Realistic Rock Geometries. Comput. Math. Appl. 59, 2305–2314.
[16] Chen, C., Packman, A. I., and Gaillard, J. F. 2008. Pore-scale Analysis of Permeability Reduction Resulting From Colloid Deposition. Geophysical Research Letters 35: L07404. https://doi.org/10.1029/2007GL033077.
[17] Chen, C., Lau, B. L. T., Gaillard, J. F. et al. 2009a. Temporal Evolution of Pore Geometry, Fluid Flow, and Solute Transport Resulting From Colloid Deposition. Water Resources Research 45: W06416. https://doi.org/10.1029/2008WR007252.
[18] Chen, C., Packman, A. I., and Gaillard, J. F. 2009b. Using X-ray Micro-Tomography and Pore-Scale Modeling to Quantify Sediment Mixing and Fluid Flow in a Developing Streambed. Geophysical Research Letters 36: L08403 https://doi.org/10.1029/2009GL037157.
[19] Chen, C., and Zhang, D. (2009), Lattice Boltzmann Simulation of the Rise and Dissolution of Two-dimensional Immiscible Droplets, Physics of Fluids, 21, 103301, doi: 10.1063/1.3253385.

[20] Chen, C., and Zhang, D. (2010), Pore-scale Simulation of Density-Driven Convection in Fractured Porous Media during Geological CO2 Sequestration, Water Resources Research, 46, W11527, doi:10.1029/2010WR009453.
[21] Chen, C., Zeng, L., and Shi, L. 2013. Continuum-Scale Convective Mixing in Geological CO2 Sequestration in Anisotropic and Heterogeneous Saline Aquifers. Advances in Water Resources 53: 175–187. https://doi.org/10.1016/j.advwatres.2012.10.012.
[22] Chen, C., Wang, Z., Majeti, D. et al. 2016. Optimization of Lattice Boltzmann Simulation With Graphics-Processing-Unit Parallel Computing and the Application in Reservoir Characterization. SPE J. 21 (4): 1425–1435. SPE-179733-PA. https://doi.org/10.2118/179733-PA.
[23] Chen, S. and Doolen, G. D. 1998. Lattice Boltzmann Method for Fluid Flows. Annu. Rev. Fluid Mech. 30: 329–364. https://doi.org/10.1146/annurev.fluid.30.1.329.
[24] Chen, H., Chen, S. and Matthaeus, W. H. 1992. Recovery of the Navier–Stokes Equations Using a Lattice-gas Boltzmann Method. Phys. Rev. A 45 (8):R5339–R5342. https://doi.org/10.1103/PhysRevA.45.R5339.
[25] Dalton, L.E., Crandall, D., Shanley, K., Gill, M., Rosenbaum, E., Moore, J., Ahmadi, G., Kutchko, B., and Chipkin, J. (2018a). Foamed Cement Generation Methods: Insights from Macro-Porosity and Void Distribution, ACI Materials Journal, 115(1) doi: 10.14359/51701101.
[26] Dalton, L.E., Brown, S., Moore, J., Crandall, D., and Gill, M. (2018b), Laboratory Foamed Cement Curing Evolution using CT Scanning, SPE Drilling and Completion, SPE-191843-PA.
[27] Dou, Z., and Zhou, Z.-F. 2013. Numerical Study of Non-uniqueness of the Factors Influencing Relative Permeability in Heterogeneous Porous Media by Lattice Boltzmann Method. Int. J. Heat Fluid Flow. 42: 23–32
[28] Donaldson, E.C. and Thomas, R.D. 1971. Microscopic Observations of Oil Displacement in Water-Wet and Oil-Wet Systems. Society of Petroleum Engineers. doi:10.2118/3555-MS
[29] Fan, M., McClure, J., Han, Y., Li, Z., and Chen, C. 2018. Interaction Between Proppant Compaction and Single-/Multiphase Flows in a Hydraulic Fracture. SPE Journal. doi:10.2118/189985-PA
[30] Fan, M., McClure, J., Han, Y., Li, Z., and Chen, C. 2017. Interaction between Proppant Packing, Reservoir Depletion, and Fluid Flow in Hydraulic Fractures. Offshore Technology Conference. doi:10.4043/27907-MS
[31] Ghassemi, A. and Pak, A. 2011. Numerical Study of Factors Influencing Relative Permeabilities of Two Immiscible Fluids Flowing through Porous Media Using Lattice Boltzmann Method, J. Petrol. Sci. Eng. 77 (1): 135–145.
[32] Goodman A, Hakala A, Bromhal G, Deel D, Rodosta T, Frailey S, et al. US DOE Methodology for the Development of Geologic Storage Potential for Carbon Dioxide at the National and Regional Scale. Int J Greenh Gas Con. 2011;5(4):952-65.
[33] Grunau, D., Chen, S., and Eggert, K. 1993. A Lattice Boltzmann Model for Multiphase Fluid Flows. Phys. Fluids A 5: 2557–2562. https://doi.org/10.1063/1.858769.
[34] Gustensen, A. K., Rothman, D. H., Zaleski, S. et al. 1991. Lattice Boltzmann Model of Immiscible Fluids. Physical Review A 43: 4320–4327. https://doi.org/10.1103/PhysRevA.43.4320.
[35] Gu, Q., Liu, H., & Zhang, Y. (2018). Lattice Boltzmann Simulation of Immiscible Two-phase Displacement in Two-dimensional Berea Sandstone. Applied Sciences, 8(9):1497

[36] Han, Y. and Cundall, P. A. 2011. Lattice Boltzmann Modeling of Pore-scale Fluid Flow Through Idealized Porous Media. Int. J. Num. Meth. Fluids 67(11): 1720–1734. https://doi.org/10.1002/fld.2443.
[37] Han, Y. and Cundall, P. A. 2013. LBM-DEM Modeling of Fluid-Solid Interaction in Porous Media. Int. J. Numer. Anal. Meth. Geomech. 37 (10): 1391–1407. https://doi.org/10.1002/nag.2096.
[38] Hao, L. and Cheng, P. 2010. Pore-scale Simulations on Relative Permeabilities of Porous Media by Lattice Boltzmann Method. Int J Heat Mass Transfer. 53(9– 10):1908–13
[39] Huang, H., Li, Z., Liu, S., and Lu, X.-Y. 2009. Shan-and-Chen-type Multiphase Lattice Boltzmann Study of Viscous Coupling Effects for Two-phase Flow in Porous Media. Int. J. Numer. Methods Fluids. 61: 341–354.
[40] Iglauer, S., C. H. Pentland, and A. Busch (2015), CO2 wettability of seal and reservoir rocks and the implications for carbon geo-sequestration, Water Resour. Res., 51, 729–774, doi:10.1002/2014WR015553.
[41] Keller, A.A, Blunt, M.J., and Roberts, P.V. 2000. Behavior of Nonaqueous Pphase Liquids in Fractured Porous Media under Two-phase Flow Conditions. Transport Porous Med. 38: 189–203
[42] Krevor, S.C.M., Pini, R., Zuo, L., and Benson, S. M. 2012. Relative Permeability and Trapping of CO_2 and Water in Sandstone Rocks at Reservoir Conditions. Water Resources Research, 48(2):W02532.
[43] Landry, C.J., Karpyn, Z.T., and Ayala, O. 2014. Relative Permeability of Homogenous-wet and Mixed-wet Porous Media as Determined by Pore-scale Lattice Boltzmann Modeling. Water Resour. Res. 50: 3672–3689. http://dx.doi.org/10.1002/2013WR015148.
[44] Lenormand, R., Touboul, E. and Zarcone, C. 1988 Numerical models and experiments on immiscible displacements in porous media, *J. of Fluid Mech.*, **189**, 165-187.
[45] Li, H., Pan, C., and Miller, C.T. 2005. Pore-scale Investigation of Viscous Coupling Effects for Two-phase Flow in Porous Media, Phys. Rev. E 72
[46] Li, R., Yang, Y.S., Pan, J., Pereira, G.G., Taylor, J.a., Clennell, B., Zou, C., 2014. Lattice Boltzmann Modeling of Permeability in Porous Materials with Partially Percolating Voxels. Phys. Rev. E 90, 033301. http://dx.doi.org/10.1103/PhysRevE.90. 033301
[47] McClure, J.E., Prins, J.F., and Miller, C.T. 2014. A Novel Heterogeneous Algorithm to Simulate Multiphase Flow in Porous Media on Multicore CPU–GPU Systems. Comput. Phys. Commun. 185: 1865–1874. http://dx.doi.org/10.1016/j.cpc.2014.03.012.
[48] Odeh, A.S. 1959. Effect of Viscosity Ratio on Relative Permeability. Trans. AIME 216: 346–352.
[49] Øren, P.E. and Bakke, S. 2003. Reconstruction of Berea Sandstone and Pore Scale Modeling of Wettability Effects. J. Pet. Sci. Eng. 39: 177–199
[50] Orr Jr, F.M. and Taber, J.J. 1984. Use of Carbon Dioxide in Enhanced Oil Recovery. Science. 224(4649):563–569.
[51] Pan, C., Luo, L., and Miller, C.T. 2006. An Evaluation of Lattice Boltzmann Schemes for Porous Medium Flow Simulation. Computers and Fluids 35 (8): 898–909. https://doi.org/10.1016/j.compfluid.2005.03.008.
[52] Ramstad, T., Øren, P., and Bakke, S. 2010. Simulation of Two Phase Flow in Reservoir Rocks Using a Lattice Boltzmann Method. Society of Petroleum Engineers, doi:10.2118/124617-PA

[53] Ramstad, T., Idowu, N., Nardi, C., and Øren, P-E. 2012. Relative Permeability Calculations from Two-phase Flow Simulations Directly on Digital Images of Porous Rocks. Transport in Porous Media. 94 (2): 487–504. https://doi.org/10.1007/s11242-011-9877-8.

[54] Rinaldi, P.R., Dari, E.A., Venere, M.J., and Clausse, A. 2012. A Lattice-Boltzmann Solver for 3D Fluid Simulation on GPU, Simul. Model. Pract. Theory. 25: 163–171. http://dx.doi.org/10.1016/j.simpat.2012.03.004.

[55] Roehm, D. and Arnold, A. 2012. Lattice Boltzmann Simulations on GPUs with ESPResSo. Eur. Phys. J.-Spec. Topics. 210 (1): 89–100. http://dx.doi.org/10.1140/ epjst/e2012-01639-6.

[56] Succi, S., Benzi, R., and Higuera, F. 1991. The Lattice-Boltzmann Equation—A New Tool for Computational Fluid Dynamics. Physica D 47: 219–230.https://doi.org/10.1016/0167-2789(91)90292-H.

[57] Succi, S. 2001. The Lattice Boltzmann Equation for Fluid Dynamics and Beyond. New York: Oxford University Press.

[58] Szulczewski, M.L., MacMinn, C.W., Herzog, H.J., and Juanes, R. 2012. Lifetime of Carbon Capture and Storage as a Climate-change Mitigation Technology. Proc Natl Acad Sci USA. 109(14):5185–5189

[59] Tsakiroglou, C., Avraam, D., and Payatakes, A. 2007. Transient and Steady-state Relative Permeabilities from Two-phase Flow Experiments in Planar Pore Networks. Adv. Water Resour. 30: 1981–1992

[60] Tudek, J., Crandall, D., Fuchs, S., Werth, C. J., Valocchi, A., Chen, Y., and Goodman, A. 2017. In Situ Contact Angle Measurements of Liquid CO_2, Brine, and Mount Simon Sandstone Core using Micro X-ray CT imaging, Sessile Drop, and Lattice Boltzmann modeling. *Journal of Petroleum Science and Engineering* **155**: 3-10. https://doi.org/10.1016/j.petrol.2017.01.047.

[61] Valvatne, P.H. and Blunt, M.J. 2004. Predictive Pore-scale Modeling of Two-phase Flow in Mixed Wet Media. Water Resour. Res. 40: 1–21

[62] Wei, N., Gill, M., Crandall, D., McIntyre, D., Wang, Y., Bruner, K., Li, X., and Bromhal, G. (2014), CO2 flooding properties of Liujiagou sandstone: influence of sub-core scale structure heterogeneity. Greenhouse Gases-Science and Technology, 2014. 4(3): p. 400-418.

[63] Yang, F., Hingerl, F.F., Xiao, X., Liu, Y., Wu, Z., Benson, M. S., and Toney, M.F. 2015. Extraction of Pore-Morphology and Capillary Pressure Curves of Porous Media from Synchrotron Based Tomography Data, Sci. Rep. 5: 10635, doi:10.1038/srep10635

[64] Yiotis, A.G., Psihogios, J., Kainourgiakis, M.E., Papaioannou, A., and Stubos, A.K. 2007. A Lattice Boltzmann Study of Viscous Coupling Effects in Immiscible Two-phase Flow in Porous Media. Colloids and Surfaces A: Physicochemical and Engineering Aspects. 300: 35–49

[65] Zhao, H., Ning, Z., Kang, Q., Chen, L., and Zhao, T. 2017. Relative Permeability of Two Immiscible Fluids Flowing through Porous Media Determined by Lattice Boltzmann Method, Int. Commun. Heat Mass 85: 53–61.